PAPER

One-step fabrication of β-Ga$_2$O$_3$–amorphous-SnO$_2$ core–shell microribbons and their thermally switchable humidity sensing properties†

Kewei Liu,* Makoto Sakurai* and Masakazu Aono*

We reported the fabrication of a highly sensitive, fast, and thermally switchable humidity sensor based on a β-Ga$_2$O$_3$–amorphous-SnO$_2$ core–shell microribbon, which was synthesized *via* a simple one-step chemical vapour deposition. The as-grown microribbons were investigated by scanning electron microscopy (SEM), energy dispersive X-ray spectroscopy (EDX), X-ray photoelectron spectroscopy (XPS), and X-ray diffraction (XRD) and the results indicated that the microribbon has a well-defined core–shell structure with β-Ga$_2$O$_3$ in the core and amorphous SnO$_2$ in the shell. At 25 °C, the conductivity of the humidity sensor at 75% relative humidity (RH) was three orders of magnitude larger than that in dry air (5% RH). The response time and recovery time were ∼28 and ∼7 s, respectively, when RH was switched between 5 and 75%. Interestingly, by changing the temperature between 12 and 40 °C at 75% RH, the sensitivity can be tuned between ∼10^5 (12 °C) and ∼10^2 (40 °C). Typical thermally switchable properties of β-Ga$_2$O$_3$–amorphous-SnO$_2$ core–shell microribbons at 75% RH were demonstrated using a heating–cooling cycle between 20 and 30 °C. The possible mechanisms have been proposed based on the novel core–shell structures and water adsorption–desorption processes. Our findings pave the way for new types of humidity sensors and thermal switches.

1. Introduction

Because of their special structural, physical and chemical characteristics, core–shell coaxial structured materials have been widely used in various fields.[1–4] In particular, these core–shell structures exhibit enhanced gas sensing properties with high sensitivity, selectivity and dynamic repeatability.[5–9] These performance enhancements are usually attributed to the heterojunction at the core–shell interface.[6–9] Recently, sensors that can respond to humidity and temperature have aroused great interest owing to their potential application to industrial processes, as well as in the fields of biomedicine and human comfort.[10–14] Different oxide materials have been investigated, such as ZnO, SnO$_2$, In$_2$O$_3$, and their compounds with a variety of shapes including wires, tubes, belts, and films. However, very little information on semiconductor humidity sensors based on core–shell structures can be found.[15]

In this work, we fabricated β-Ga$_2$O$_3$–amorphous-SnO$_2$ core–shell microribbons using a simple one-step chemical vapour deposition (CVD).[16] SnO$_2$ is the most commonly used material for gas sensors and has a good sensitivity to relative humidity (RH) in air at low temperatures.[14,17–20] On the other hand, β-Ga$_2$O$_3$, owing to its good physical, chemical and thermally stable properties, has a wide range of applications, such as in photodetectors and high-temperature gas sensors.[21–24] Therefore, their combination as a core–shell structure is expected to exhibit novel properties in the gas sensor field, such as tunable sensitivity and selectivity for different gases, and a wide operating temperature range. Moreover, the difference in work function between Ga$_2$O$_3$ and SnO$_2$ can induce the depletion region in SnO$_2$, resulting in a decrease in background signal intensity and the increase in response speed, which play an important role in detecting reducing gas. β-Ga$_2$O$_3$–SnO$_2$ core–shell microribbons fabricated by one-step CVD have the following advantages over those fabricated by the two-step method, in which the core and shell grow independently.[25–27] The one-step method saves time and cost in the fabrication process. More interestingly, the SnO$_2$ shell in the present system has an amorphous structure and a large protrusion. Because these properties produce large active channels and high surface areas, which are required for gas sensors,[28] the humidity sensor based on the Ga$_2$O$_3$–SnO$_2$ core–shell structure showed good humidity-sensing performance at room temperature. The mechanism of the RH- and temperature-dependent sensitivity is discussed in detail.

2. Experimental

Synthesis of β-Ga$_2$O$_3$–amorphous-SnO$_2$ core–shell microribbons

The β-Ga$_2$O$_3$–amorphous-SnO$_2$ core–shell microribbons used in this study were synthesized inside a ceramic boat in a horizontal

International Center for Materials Nanoarchitectonics (MANA), National Institute for Materials Science (NIMS), Tsukuba 305-0044, Japan. E-mail: Liukewei2007@yahoo.com.cn; Liu.Kewei@nims.go.jp; Sakurai.Makoto@nims.go.jp; Aono.Masakazu@nims.go.jp

tube furnace by CVD. A mixture of highly pure (99.999%) Ga_2O_3 powder, (99.999%) SnO_2 powder and (99.999%) graphite powder with a weight ratio of 1 : 1 : 2 Ga_2O_3–SnO_2–C was used as the source. A ceramic boat containing the Ga_2O_3–SnO_2–C powder was placed in a horizontal tube furnace (see Fig. S1†). The temperature was first raised to 200 °C in a vacuum for 10 min to remove the water and adsorption gas in the source. After that, the temperature was increased to 990 °C with a flow of highly pure argon mixed with 4% oxygen as the protective medium and carrier gas with a pressure of 9.0×10^2 Pa. The temperature was maintained for 60 min and then naturally cooled to room temperature. β-Ga_2O_3–amorphous-SnO_2 core–shell microribbons were grown at the end of the ceramic boat.

Characterization of the samples

The structural information and surface properties of the microribbons were obtained using scanning electron microscopy (SEM) (Hitachi S-4800) with energy dispersive X-ray spectroscopy (EDX), X-ray photoelectron spectroscopy (XPS) (Thermo Fisher Scientific, Theta Probe) and X-ray diffraction (XRD) (Rigaku AFC7R).

Device fabrication and characterization

The β-Ga_2O_3–amorphous-SnO_2 core–shell microribbon was first transferred from the ceramic boat to the flat substrate by using tweezers and a metal wire with a sharp tip. The microribbon lies flat on the substrate. The Au electrodes with a thickness of 500 nm were made by thermal evaporation through a shadow mask onto the substrate at room temperature. In order to well understand the humidity sensing mechanism and to investigate the effect of the core–shell structure, β-Ga_2O_3-microribbon- and single-crystal-SnO_2-microwire-based devices were fabricated using the same method as reference. The current–voltage (I–V) and thermally switchable humidity sensing properties of an individual β-Ga_2O_3–amorphous-SnO_2 core–shell microribbon-based device were measured in air using a picoammeter (Keithley, model 6458) under different conditions (see Fig. S2†).

3.   Results and discussion

Structural and morphology characterization of β-Ga_2O_3–amorphous-SnO_2 core–shell microribbons

Fig. 1(a) shows a low-magnification SEM image of as-grown Ga_2O_3–SnO_2 microribbon core–shells, and it reveals that all the specimens display a ribbon morphology with a length of up to 3–5 mm. The as-grown microribbons have a rectangular cross-section with typical widths of 8–12 μm and thicknesses of 1–2 μm (see Fig. 1(b)). The inset in Fig. 1(b) shows the roughness of the surface. Fig. 1(c) shows a SEM image of the microribbon and an EDX line scan was taken along the dotted red line. The spatial distributions of Ga, O and Sn indicated that the microribbons have a well-defined core–shell structure with Ga_2O_3 in the core and SnO_2 in the shell. The thickness of the SnO_2 shell is approximately 300 nm as shown in Fig. 1(c).
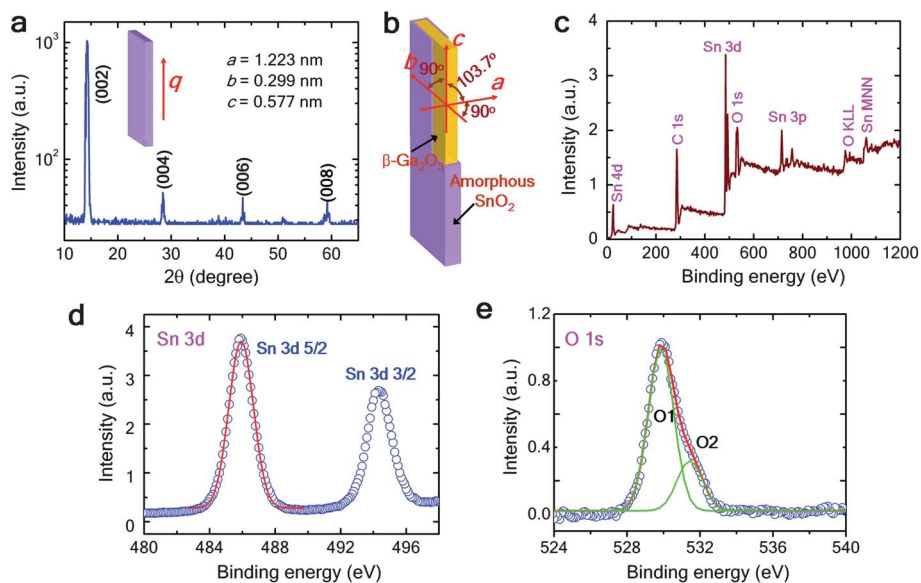
   To further investigate the crystal structure of core–shell microribbons, XRD measurement was carried out on a single microribbon. In particular, Fig. 2(a) shows the XRD patterns
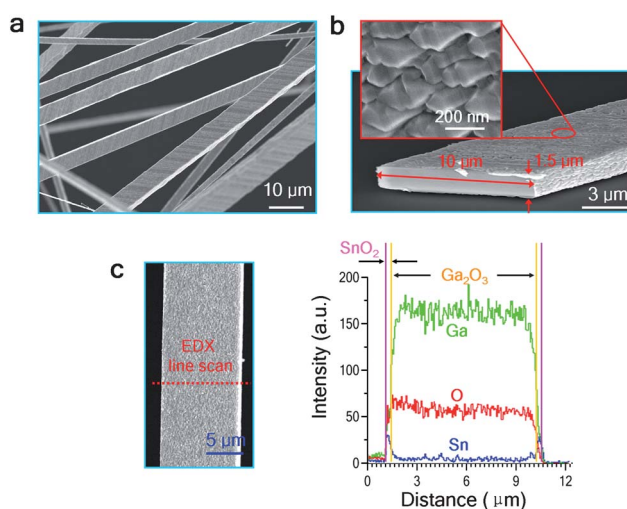
Fig. 1 SEM images of as-grown β-Ga_2O_3–amorphous-SnO_2 core–shell microribbons with (a) low and (b) high magnification. (c) EDX line scanning concentration profiles of β-Ga_2O_3–amorphous-SnO_2 core–shell microribbons.

with the scattering vector q parallel to the ribbon axis. In this figure, the diffraction peaks at $2\theta = 14.3, 28.4, 43.4$ and $59.2°$ can be associated with the diffraction from the (002), (004), (006) and (008) planes of the β-Ga_2O_3 with a monoclinic structure. This result suggests that the length direction is along the c-axis of β-Ga_2O_3. Additionally, the absence of the diffraction peak related to SnO_2 indicates that SnO_2 exists as an amorphous phase. The lattice parameters of β-Ga_2O_3 calculated from the XRD data are: $a = 1.223$ nm, $b = 0.229$ nm, $c = 0.577$ nm and $\beta = 103.7°$, which are consistent with the standard values of the bulk material (JCPDS 431012). This consistency confirmed that almost no Sn element has been doped into the lattice of β-Ga_2O_3. The X-ray diffraction patterns obtained using the four-axis XRD system determines the orientation of the β-Ga_2O_3 core structure, as shown in Fig. 2(b).

   XPS was used to investigate the surface composition of as-grown β-Ga_2O_3–amorphous-SnO_2 core–shell microribbons. Fig. 2(c) shows the XPS profiles of the sample scanned in the range of 0–1200 eV. The binding energies are calibrated by taking the carbon C 1s peak (284.6 eV) as reference. All the peaks can be ascribed to Sn, O, and C, as labeled in Fig. 2(c). No Ga element peak was observed within the sensitivity range of the technique in our sample. This result confirmed that the microribbon was covered completely by the SnO_2 shell, which is consistent with the model in Fig. 2(b). Fig. 2(d) shows the double spectral lines of Sn 3d at binding energies of 485.9 eV (Sn $3d_{5/2}$) and 494.3 eV (Sn $3d_{3/2}$) with a spin–orbit splitting of 8.4 eV, which coincides with the findings for the Sn^{4+} ion bound to oxygen in the SnO_2 matrix.[29] The peak of Sn $3d_{5/2}$ shows only one symmetric component without a shoulder peak. The O 1s peak can be decomposed into two components at 531.1 and 532.7 eV, as shown in Fig. 2(e). The low-energy peak at 531.1 eV corresponds to O^{2-} from the rutile structure of the SnO_2 lattice, whereas the peak at 532.7 eV can be ascribed to the presence of tin hydroxide on the surface of amorphous SnO_2.[29] The results of the structural analysis demonstrate that β-Ga_2O_3–amorphous-SnO_2 core–shell microribbons were fabricated by the simple one-step CVD,

This journal is © The Royal Society of Chemistry 2012

*J. Mater. Chem.*, 2012, **22**, 12882–12887 | 12883

Fig. 2 (a) The XRD patterns of an as-grown single microribbon with the scattering vector q parallel to the rod axis. (b) The schematic structure of the β-Ga_2O_3–amorphous-SnO_2 core–shell microribbon. (c) XPS spectra of as-grown microribbons scanned from 0 to 1200 eV. (d) Binding energy of Sn 3d. (e) Binding energy of O 1s.

which produces a unique structure different from the coaxial structure fabricated by the two-step method.[25–27]

Humidity sensing properties

To examine the humidity sensing properties of the β-Ga_2O_3–amorphous-SnO_2 core–shell microribbons, humidity sensors were fabricated and their properties investigated under different conditions. A single β-Ga_2O_3–amorphous-SnO_2 core–shell microribbon with a width of 10 μm and a thickness of 1 μm was selected to fabricate the device, because a micro-sized structure is easy to manipulate and gas molecules have a better chance of being adsorbed by this larger surface area. 500 nm thick Au was evaporated at the electrodes and the distance between the two Au electrodes was 200 μm. Fig. 3(a) shows the $I–V$ curves of the core–shell microribbon-based humidity sensor in dry air (5% RH) and 75% RH air at 25 °C. In both RH atmospheres, the $I–V$ curves of the device exhibit good linear behavior, which proves a good ohmic contact between the microribbon and the Au electrodes. At the same time, the resistance of the microribbon in dry air was calculated to be about 3.5×10^{12} Ω, which is ~3 orders of magnitude larger than that in 75% RH air (1.1×10^9 Ω). Evidently, the resistance of the microribbon was strongly affected by the water vapor in air. The top and bottom insets in Fig. 3(a) show the $I–V$ curves of two control devices based on β-Ga_2O_3 microribbons and single-crystal SnO_2 microwires, respectively. The measured conditions for two control devices are the same with those for the β-Ga_2O_3–amorphous-SnO_2 core–shell microribbon sensor. It can be seen that the β-Ga_2O_3 microribbon has an ultra-high resistance (under the instrumental limit) at both 5% and 75% RH, which can be attributed to the lower carrier density of the Ga_2O_3 microribbon. For a single-crystal SnO_2 microwire, the $I–V$ curves of the device exhibit good linear behavior and the resistance was calculated to be about 9.1×10^6 Ω in dry air, which is ~6 orders of magnitude smaller
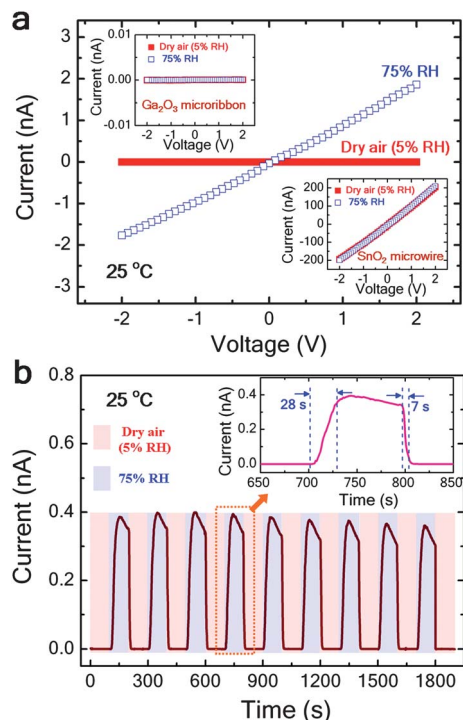
**Fig. 3** (a) The $I–V$ curves of the core–shell microribbon-based humidity sensor in dry air (5% RH) and 75% RH air at 25 °C. The top and bottom insets show the $I–V$ curves of the Ga_2O_3 microribbon and SnO_2 microwire, respectively, which are used as control samples. Both control samples have neglectable humidity sensing property at 25 °C. (b) The dynamic response of the β-Ga_2O_3–amorphous-SnO_2 core–shell microribbon sensor for the detection of 75% RH air. The inset shows that the response time and recovery time (defined as the time required to reach 90% of the final equilibrium value) were ~28 and ~7 s, respectively.

than that of the core–shell microribbon (3.5×10^{12} Ω). However, the difference in resistance can be neglectable when measured at 5% and 75% RH. The lower resistance and neglectable humidity sensing properties of the single-crystal SnO_2 microwire should be associated with surface properties and the low ratio of surface to volume. Therefore, it can be concluded that the ultra-large increase in conductivity of the β-Ga_2O_3–amorphous-SnO_2 microribbon in humid air can be attributed to the amorphous phase of SnO_2, core–shell structures, and water layers, which will be discussed later. The dynamic response of the β-Ga_2O_3–amorphous-SnO_2 core–shell microribbon sensor for the detection of 75% RH air is shown in Fig. 3(b). The sensor was operated at 25 °C and periodically exposed to dry air flow and 75% RH air flow. It can be seen that there are few changes in the peak values in the curves for nine cycles, implying the good reproducibility of the sensor. Furthermore, the response time and recovery time (defined as the time required to reach 90% of the final equilibrium value) were ~28 and ~7 s, respectively, when RH was switched between 5 and 75% (see inset in Fig. 3(b)). The response time and recovery time are shorter than those in most previous reports.[11–14]

The sensitivity S of the sensor is defined as the ratio of electrical resistance in dry air to that in humid air ($R_{dry\ air}/R_{humid\ air}$). Under a constant voltage, S can be expressed as

$$S = \frac{I_{humid\ air}}{I_{dry\ air}} \quad (1)$$

where $I_{dry\ air}$ and $I_{humid\ air}$ represent the currents of the sensor in dry air and humid air under a constant voltage, respectively. The sensitivity at different temperatures as a function of RH is shown in Fig. 4. At 12 °C, the sensitivity increased largely with increasing RH from 15 to 55%. As RH was increased further, the sensitivity increased slightly and reached saturation at ~10^5. The saturation behavior under a high RH at 12 °C can be attributed to the fact that large numbers of water molecules have adsorbed on the microribbon already at 55% RH and the further increase in RH cannot realize a large change in conductivity. At 20 °C, the sensitivity increased largely with increasing RH from 23 to 85% and no saturation can be observed. As for the operating temperatures at 30 and 38 °C, the increase in sensitivity slowed
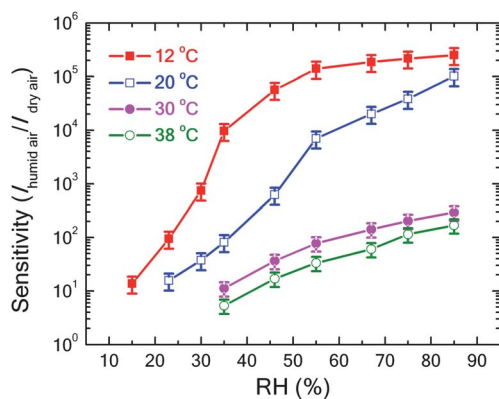
down with increasing RH. Interestingly, at a high RH, the core–shell microribbon humidity sensor is very sensitive to temperature, and the sensitivity can be decreased by 2–3 orders with increasing temperature from 20 to 30 °C.

To further investigate the thermal effect on the sensitivity, the temperature dependence of the sensor current in 75% RH air is shown in Fig. 5(a). Although a large current was observed below 20 °C, a sharp decrease in sensor current was observed at 24 ± 4 °C, and the current became almost constant above 33 °C. The change in current was reversible with temperature. The current response to the temperature change suggests that microribbons have thermal switchable properties in 75% RH air. Furthermore, the sensor in dry air showed almost no changes in current with increasing temperature from 12 to 40 °C (see inset in Fig. 5(a)). By switching the temperature of the microribbon between 20 and 30 °C, the current cycled between a relatively high value at 20 °C (~10 nA) and a very small value at 30 °C (~0.02 nA), as shown in Fig. 5(b). The results demonstrate the reversibility and repetition of the resistivity of β-Ga_2O_3–amorphous-SnO_2 core–shell microribbons at a high RH in heating and cooling processes.

β-Ga_2O_3–amorphous-SnO_2 core–shell microribbons show a high sensitivity and a fast response to water vapor near room temperature. To obtain good understanding of the mechanisms of their performance, a model based on the surface and heterojunction effect was proposed, as shown in Fig. 6. SnO_2 is an n-type semiconductor with a band gap of 3.6 eV and a work function of 4.7 eV, and β-Ga_2O_3 is an n-type semiconductor with a band gap of 4.7 eV and a work function of 5.0 eV.[30–32] At the heterojunction
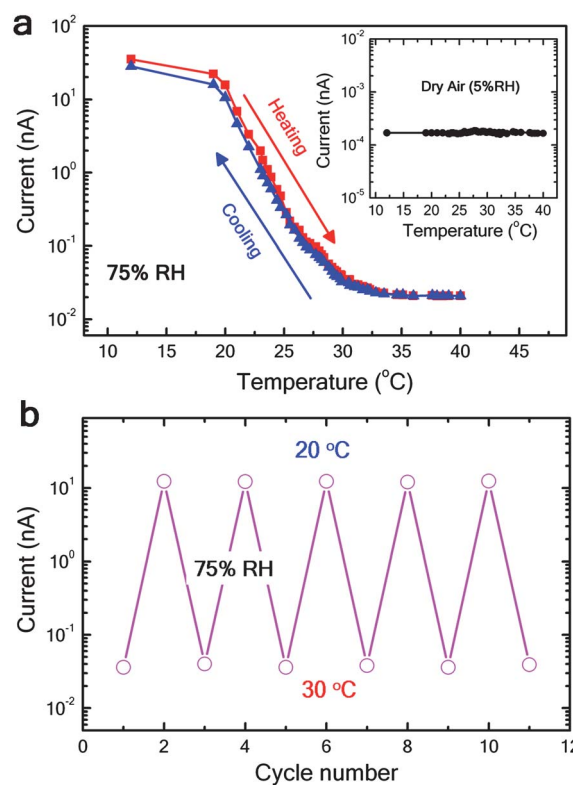
Fig. 5 (a) The temperature dependence of the sensor current in 75% RH air at $V = 1$ V. The inset shows the temperature dependence of the sensor current in dry air. (b) Dependence of the sensor current in 75% RH on the temperature switched between 20 and 30 °C.

Fig. 4 The sensitivity at different temperatures as a function of RH at different operation temperatures of 12 °C (red solid square line), 20 °C (blue open square line), 30 °C (pink solid circle line) and 38 °C (green open circle line).

This journal is © The Royal Society of Chemistry 2012

J. Mater. Chem., 2012, **22**, 12882–12887 | 12885

between amorphous SnO_2 and β-Ga_2O_3, electrons transfer from SnO_2 to Ga_2O_3 owing to the difference between their energy positions, and barriers and depletion layers are formed. When the sensor is exposed to dry air (see Fig. 6(a)), some oxygen molecules will adsorb onto the surface, and at the interface and grain boundaries of amorphous SnO_2 shells. Adsorbed oxygen molecules capture free electrons from the conduction band in n-type SnO_2 and form oxygen ions according to

$$O_2 + e^- = O_2^- \qquad (2)$$

Therefore, a depletion layer with a low conductivity is created near the surface, leading to a decrease in carrier concentration. Because Ga_2O_3 is completely covered by SnO_2 and there is no etching of the SnO_2 shell before the Au deposition, the current mainly flows through the shell. Therefore, the temperature dependence and strong RH dependence of the humidity sensor result from the transport through SnO_2 shells in a humid atmosphere. The main effect of the Ga_2O_3 core (or the core–shell heterojunction) is that it decreases the carrier density in the SnO_2 shell, which is similar to that of the gate voltage in a field effect transistor.

When the sensor is exposed to humid air (see Fig. 6(b)), H_2O is physisorbed on the oxide surface in molecular forms and chemisorption hardly takes place owing to the low operating temperature (<50 °C).[11–14] At a low RH, water molecules replace O^{2-}, therefore releasing electrons from O^{2-}. The increase in free electron concentration results in a decrease in barrier height at the interface of the Ga_2O_3–SnO_2 heterojunction and the surface of SnO_2. Meanwhile, electrons are attracted to the surface by the preferential alignment of water dipoles.[11–13] Because of the high carrier concentration near the surface of SnO_2, the conductivity of the humidity sensor increases markedly. Water adsorbed at grain boundaries of the SnO_2 shell assists the current flowing through the boundary. With an increase in RH, subsequent layers of water molecules are physically adsorbed on the first water layer, as shown in Fig. 6(b). Protons act as charge carriers, transporting charges between physisorbed water molecules on the SnO_2 surface.[11–13] With further increase in RH, in addition to the protonic conduction in adsorbed water layers, electrolytic conduction takes place in liquid water, which condenses in capillary pores. The formation of such pores is due to nanoscale grain boundaries of amorphous SnO_2 shells.[33] Because there are several mechanisms underlying the conduction increase in humid

air as mentioned above, the resistance changes nonlinearly with RH and its sensitivity is very high. The water, adsorbed in molecular form, is easily desorbed from the surface owing to its weak bonding with the surface, which can be used to explain the quick response and recovery to humidity. Additionally, the depletion layers at the heterojunction and surface are formed by the movement of electrons immediately after the desorption of water molecules, so the humidity sensor can quickly return to its original high resistance state.

Since the number of water molecules on SnO_2 shells determines sensor current, it is instructive to compare the temperature dependent sensitivity of the sensor to the water physisorption isotherms on the SnO_2 surface,[34] in which the number of water molecules on the oxide surface is plotted against the pressure of H_2O vapor at a constant temperature. At low temperatures ($T <$ 20 °C), the large increase in sensor current is consistent with the high sensitivity of the isotherms: monolayer coverage is achieved at a very low pressure of H_2O gas (very low RH). As temperature increases from 20 to 40 °C, monolayer coverage begins to require a higher H_2O gas pressure (high RH) in the isotherms, and the decrease in sensitivity agrees with the decrease in sensor current under a constant RH. The saturation of the sensor current at approximately 40 °C is in good agreement with the desorption temperature of physically adsorbed water on SnO_2 (~40 °C).[35] Because temperature determines the ratio of adsorption to desorption of water molecules on a SnO_2 surface under equilibrium condition, the thermal switching of the sensor occurs without hysteresis, as shown in Fig. 5(a).

4. Conclusions

In summary, we have demonstrated the one-step fabrication of β-Ga_2O_3–amorphous-SnO_2 core–shell microribbons by CVD. These microribbons have a very high sensitivity to humidity with quick response and recovery near room temperature. The good sensing performance of the β-Ga_2O_3–amorphous-SnO_2 core–shell microribbon humidity sensor can be attributed to the large surface area of the amorphous-SnO_2 shell and the heterojunction between Ga_2O_3 and SnO_2. The fast physisorption of water molecules and the fast formation of depletion layers in the sensor explain the quick response and recovery to humidity. More interestingly, typical thermally switchable properties of the microribbons were observed at 75% RH using a heating–cooling cycle between 20 and 30 °C. The large change in resistance is due to the temperature dependent adsorption of water molecules
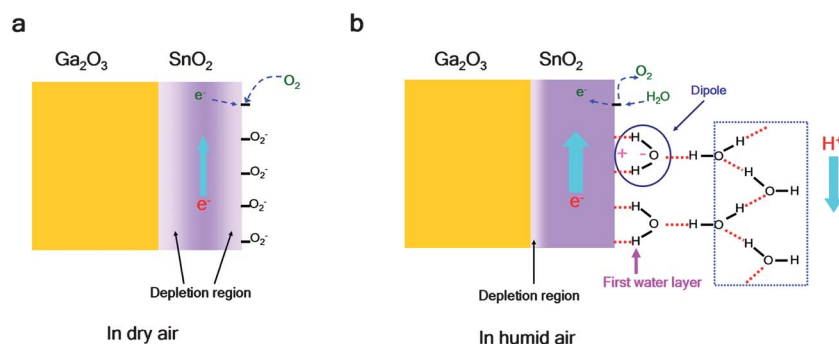

Fig. 6 Conductivity model of the β-Ga_2O_3–amorphous-SnO_2 core–shell microribbon in (a) dry air and (b) humid air.

onto the SnO_2 surface. The results pave the way for the development of new types of humidity sensors and thermal switches. Future work will focus on studying the sensing behavior of microribbons for other reducing gases and on further improving the performance of devices.

Acknowledgements

References

1 B. Tian, X. Zheng, T. J. Kempa, Y. Fang, N. Yu, G. Yu, J. Huang and C. M. Lieber, *Nature*, 2007, **449**, 886.
2 K. Wang, J. Chen, W. Zhou, Y. Zhang, Y. Yan, J. Pern and A. Mascarenhas, *Adv. Mater.*, 2008, **20**, 3248.
3 S. Choi, J. Y. Park and S. S. Kim, *Nanotechnology*, 2009, **20**, 465603.
4 J. Park and S.-W. Kim, *J. Mater. Chem.*, 2011, **21**, 3745.
5 Y. J. Chen, C. L. Zhu, L. J. Wang, P. Gao, M. S. Cao and X. L. Shi, *Nanotechnology*, 2009, **20**, 045502.
6 I. S. Hwang, S. J. Kim, J. K. Choi, J. Choi, H. Ji, G. T. Kim, G. Cao and J. H. Lee, *Sens. Actuators, B*, 2010, **148**, 595.
7 J. Y. Park, S.-W. Choi and S. S. Kim, *J. Phys. D: Appl. Phys.*, 2011, **44**, 205403.
8 Y. J. Chen, G. Xiao, T. S. Wang, F. Zhang, Y. Ma, P. Gao, C. L. Zhu, E. Zhang, Z. Xu and Q. H. Li, *Sens. Actuators, B*, 2011, **156**, 867.
9 X. Xue, L. Xing, Y. Chen, S. Shi, Y. Wang and T. Wang, *J. Phys. Chem. C*, 2008, **112**(32), 12157.
10 B. Cheng, B. Tian, C. Xie, Y. Xiao and S. Lei, *J. Mater. Chem.*, 2011, **21**, 1907.
11 B. M. Kulwicki, *J. Am. Ceram. Soc.*, 1991, **74**(4), 697.
12 Z. Chen and C. Lu, *Sens. Lett.*, 2005, **3**, 274.
13 E. Traversa, *Sens. Actuators, B*, 1995, **23**, 135.
14 Q. Kuang, C. Lao, Z. L. Wang, Z. Xie and L. Zheng, *J. Am. Chem. Soc.*, 2007, **129**, 6070.
15 L. Gu, K. Zheng, Y. Zhou, J. Li, X. Mo, G. R. Patzke and G. Chen, *Sens. Actuators, B*, 2011, **159**, 1.
16 K. W. Liu, M. Sakurai, M. Y. Liao and M. Aono, *J. Phys. Chem. C*, 2010, **114**, 19835.
17 *Functional Nanomaterials*, ed. K. E. Geckeler and E. Rosenberg, American Scientific Publ, Valencia, USA, 2006, ch. 30.
18 M. Law, H. Kind, B. Messer, F. Kim and P. Yang, *Angew. Chem., Int. Ed.*, 2002, **41**, 2405.
19 L. L. Fields, J. P. Zheng, Y. Cheng and P. Xiong, *Appl. Phys. Lett.*, 2006, **88**, 263102.
20 Y. Cheng, P. Xiong, L. Fields, J. P. Zheng, R. S. Yang and Z. L. Wang, *Appl. Phys. Lett.*, 2006, **89**, 093114.
21 M. Ogita, K. Higo, Y. Nakanishi and Y. Hatanaka, *Appl. Surf. Sci.*, 2001, **175–176**, 721.
22 Z. Liu, T. Yamazaki, Y. Shen, T. Kikuta, N. Nakatani and Y. Li, *Sens. Actuators, B*, 2008, **129**, 666.
23 Z. R. Dai, Z. W. Pan and Z. L. Wang, *J. Phys. Chem. B*, 2002, **106**, 902.
24 Y. Li, T. Tokizono, M. Liao, M. Zhong, Y. Koide, I. Yamada and J. J. Delaunay, *Adv. Funct. Mater.*, 2010, **20**, 3972.
25 C. Jin, H. Kim, K. Baek, H. W. Kim and C. Lee, *Cryst. Res. Technol.*, 2010, **45**, 199.
26 L. Mazeina, Y. N. Picard, S. I. Maximenko, F. K. Perkins, E. R. Glaser, M. E. Twigg, J. A. Freitas Jr and S. M. Prokes, *Cryst. Growth Des.*, 2009, **9**, 4471.
27 Y. Jang, W. Kim, D. Kim and S. Hong, *J. Mater. Res.*, 2011, **26**, 2322.
28 H. F. Lu, F. Li, G. Liu, Z. G. Chen, D. W. Wang, H. T. Fang, G. Q. Lu, Z. H. Jiang and H. M. Cheng, *Nanotechnology*, 2008, **19**, 405504.
29 D. Yang, I. Kamienchick, D. Y. Youn, A. Rothschild and I. Kim, *Adv. Funct. Mater.*, 2010, **20**, 4258.
30 J. Robertson, *J. Non-Cryst. Solids*, 2008, **354**, 2791.
31 M. Batzill and U. Diebold, *Prog. Surf. Sci.*, 2005, **79**, 47.
32 L. Fu, Y. Liu, P. Hu, K. Xiao, G. Yu and D. Zhu, *Chem. Mater.*, 2003, **15**, 4287.
33 P. Chauhan, S. Annapoorni and S. K. Trikha, *Thin Solid Films*, 1999, **346**, 266.
34 K. Morishige, S. Kittaka and T. Morimoto, *Surf. Sci.*, 1981, **109**, 291.
35 E. W. Thornton and P. G. Harrison, *J. Chem. Soc., Faraday Trans. 1*, 1975, **71**, 461.

This journal is © The Royal Society of Chemistry 2012

J. Mater. Chem., 2012, **22**, 12882–12887 | 12887